Morphological Multiscale Shape Analysis of Light Micrographs

Volker Metzler[1], Thomas Lehmann[2], and Til Aach[1]

[1]Institute for Signal Processing, Medical University of Lübeck, Germany

[2]Institute of Medical Informatics, Aachen University of Technology, Germany

ABSTRACT

Shape analysis of light–micrographs of cell populations is important for cytotoxicity evaluation. This paper presents a morphological method for quantitative analysis of shape deformations of cells in contact to a biomaterial. After illumination normalization, a morphological multiscale segmentation yields separated cells. Shape deformation, and hence, toxicity of the substance under scrutiny, is quantified by means of compactness distribution and pattern spectrum of the population. Since the logarithmic image model is applicable to transmitted light, illumination normalization is achieved by removing the illumination component from the log–image by a tophat transform utilizing a large reconstruction filter. Subsequent thresholding and noise filtering yields connected binary cells, which are segmented by a marker–based, multiscale approach. For this, size–specific marker scales are generated removing noise and false markers. Each cell is now represented by an isolated marker. Converse integration of marker scales is performed by successive reconstruction of the original cell shapes, preventing merging of markers. Our method yields reasonable cell segmentations that go along with cell morphology even for differently sized and very distinct shapes. The obtained quantitative data is significantly correlated to the toxicity of the substance to be evaluated. Currently, the method is used for extensive biocompatibility tests.

Keywords: Shape analysis, mathematical morphology, scale–space, light micrograph, logarithmic image model, quantitative cytology, biomaterials, cytotoxicity, pattern spectrum

1. INTRODUCTION

Quantitative analysis of image content is an important application in medical image processing. Particularly reliable automatic analysis of cytological or histological micrographs is demanded for clinical routine purposes.[1,2] Many of such tasks require shape analysis of cell populations to assess their condition. Especially in biomaterial research, the cytotoxicity of medical devices (i.e. implants or catheters) is evaluated by means of morphological changes of standard cells (mouse fibroblasts) that were in contact with the biomaterial. Toxic effects on vital cells commonly result in a rounding and shrinking of cells that usually are more extended and have differentiated contours.[3] Currently, this process is done qualitatively by microscopic observation of cell deformation. The observed effects can be recorded only descriptively as deviations from normal cell morphology. This leads to the well known ambiguities in interpretation and comparison of biological studies. To overcome the limitations of such qualitative or semi–quantitative studies, we developed a robust computer–assisted method for shape analysis of single–layered confluent cell populations. The method consists of three stages: illumination normalization, morphological segmentation of cells, and quantification of shape deformation.

Common effects in light microscopy are low–frequency intensity gradients across the sample. These might result from inhomogeneous illumination caused by light sources or inhomogeneous dye concentration in the tissue. In the case of diascopic imaging variations of slice thickness of the sample additionally might cause inhomogeneities of captured objects. Such effects can be neglected for visual inspection, but for automatic quantitative analysis of the samples inhomogeneous illumination components may cause mayor difficulties and require advanced segmentation techniques. Usually, additive illumination components are assumed, which can be normalized by local filtering. Since in diascopic imaging object information and illumination are related multiplicatively, we use the logarithmic image model[4] for removing the illumination component by linear signal decomposition.[5] This technique has been applied

Correspondence address: Volker Metzler, Institut für Signalverarbeitung, Medizinische Universität zu Lübeck, Ratzeburger Allee 160, D–23538 Lübeck, Germany, Phone:+451–3909–559, Fax:+451–3909–555, metzler@isip.mu-luebeck.de

In *Nonlinear Image Processing XI*, Edward R. Dougherty, Jaakko T. Astola, Editors, Proceedings of SPIE Vol. 3961 (2000) • 0277-786X/00/$15.00

successfully to illumination invariant scene analysis[6] and removement of signal–dependent noise.[7] However, linear low–pass filtering always removes important object information and parts of cytological images contain no object information at all. Therefore we perform illumination normalization by a tophat transform utilizing morphological reconstruction[8] (Sec. 2).

The spatial frequencies of micrographs are used to examine information on distances between cells and their position in the image. Such information is less useful in quantitative cytology. The structural analysis of cytological images often is performed by means of morphological filters[9–12] because of their shape–, rather than frequency–oriented operations.[13] Morphological, or more generally, nonlinear approaches are well suited for shape description[14] and decomposition[15,16] leading to multiscale shape representations.[17,18] Because vital mouse fibroblasts vary significantly in shape and size we use a morphological approach to segment connected cells. The two–stage multiscale algorithm is based on morphological information of the illumination–normalized binary image. First the image is decomposed into size–specific scales, each of which carrying markers representing separate cells. Thereafter, the original shapes are reconstructed successively from the markers without merging them again (Sec. 3).

Shape is (besides color) the most important feature to assess the condition of cytological structures. In the case of biomaterial evaluation, toxicity is quantified as a measure of shape deformation relative to the shape of vital cells. However, among common similarity measures for graylevel images[19] only few are applicable for binary images. E.g. the compactness of an object represents its similarity to an ideal circle.[20] Increasing toxicity leads to rounding of fibroblasts. Therefore the compactness distribution of a population was chosen as shape descriptor. Moreover, the morphological concept of pattern spectrum is used for quantifying shape deformations.[15] The obtained parameters of cytotoxicity were verified with fibroblasts treated with defined concentrations of toxical reference substances and turned out to be significant for the different toxicity stages (Sec. 4).

2. ILLUMINATION NORMALIZATION

Inhomogeneous illumination is a common problem in quantitative microscopy. Additive illumination influences can be normalized by removing local means or utilizing derivatives for object detection.[21] However, in the case of diascopic micrographs we deal with a multiplicative relationship between the mainly high–frequency object information and the (unwanted) rather low–frequency variations of illumination. This leads to the use of the logarithmic image model, which is applicable to transmitted light[4] and is appropriate for removing multiplicative illumination components. Here, the image function $F(x,y)$ is regarded as the intensity of light passing through a light absorbing sample. This relation can be written as

$$F(x,y) = (g - A(x,y)) \cdot I(x,y) \tag{1}$$

where $A(x,y)$ and $I(x,y)$ denote the wanted absorption and microscope illumination, respectively. The constant g represents the maximum digital intensity value, which is 255 for 8–bit images. According to the log–image model, illumination influences can be normalized by a signal decomposition into a high–frequency object component and a low–frequency illumination component in the log–domain.[5] Hence, the absorption component $A(x,y)$ can be extracted by apply a linear low–pass filter in the log–domain and subtracting it from the log–image. Final exponentiation and subtraction from g yields the absorption:

$$A(x,y) = g - \exp\left(\log(F(x,y)) - \log(I(x,y))\right) \tag{2}$$

Linear low–pass filtering for identification of $\log(I(x,y))$ also removes object information. In our case, better absorption images were obtained by using a morphological filter with a large structuring element. Due to their nonlinear properties, such filters remove less low–frequency object information from the absorption component. Consequently, $g - A(x,y)$ is identified in the log–domain by a tophat transform utilizing a large closing–by–reconstruction filter. The scheme in Fig. 1 depicts the technique to obtain the absorption component $A(x,y)$ from $F(x,y)$, which is said to be illumination normalized, since it is $g - A(x,y) = F(x,y)/I(x,y)$.

Morphological illumination correction of dark objects on light background usually is done by a tophat of closing (black–tophat),[8] especially for real–life scenes where illumination normalization yields the reflectance component containing rather high–frequent object information.[22] For pixels in cytological images belonging to the background, absorption equals zero, i.e. $F(x,y) = I(x,y)$. Therefore closing will lead to $F(x,y) < I(x,y)$ resulting in a false

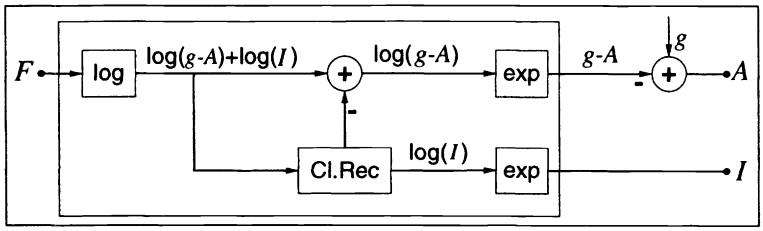

Figure 1. Illumination normalization of a diascopic micrograph $F = (g - A) \cdot I$. The initial logarithm transforms the multiplicative relation between A and I into an additive one. Reconstruction filtering identifies I and the tophat yields $g - A$, where g is the maximum illumination.

absorption $A(x, y) > 0$. Since background pixels carry no absorption information, a filter is needed to identify background as pure illumination. A closing–by–reconstruction results in an optimal background illumination component. Pixels in the resulting absorption component belonging to an object have values $A(x, y) > 0$ whereas background pixels carry $A(x, y) = 0$. Hence, with a constant global threshold $t = 1$ the object shapes in each cytograph can easily be determined.

The effect of our illumination normalization is illustrated by Fig. 2. Binarization of absorption (e) yields much clearer shapes then direct thresholding (b).

3. MORPHOLOGICAL SEGMENTATION

Because the minimum size of cells is known a priori, binary noise is removed initially from the micrographs. Thereafter the cell population is segmented by the multiscale approach.

3.1. Binary noise filtering

Binarized samples as the one shown in Fig. 2 (e) have to be cleaned from noise prior to segmentation of the population. Besides technical sources, noise also result from detection errors, cell particles, or other artifacts in the sample.

Classification of binary segments into cells and noise is done with respect to the known minimum size of cells. The digital images (in 100 times microscopical magnification) display an area of $422.4\mu\text{m} \times 607.3\mu\text{m}$ which covers in total 0.256mm^2 ($512 \times 736 = 376,832$ pixels). Filtering of $A(x, y)$ is performed by the double reconstruction filter:

$$\Psi_\sigma^\infty(A) := \mathbf{C}_\sigma^\infty\left(\mathbf{O}_\sigma^\infty(A)\right) \tag{3}$$

consisting of successive application of opening– and closing–by–reconstruction:

$$\mathbf{O}_\sigma^\infty(A) := \mathbf{D}_\sigma^\infty\left(\mathbf{E}_\sigma^n(A), A\right) \tag{4}$$

$$\mathbf{C}_\sigma^\infty(A) := \mathbf{E}_\sigma^\infty\left(\mathbf{D}_\sigma^n(A), A\right) \tag{5}$$

where $\mathbf{D}_\sigma^m$ and $\mathbf{E}_\sigma^n$ denote m–fold dilation and n–fold erosion, respectively. The exponent ∞ indicates operating until idempotency.[23] $\mathbf{D}(A, M)$ and $\mathbf{E}(A, M)$ denote conditional dilation and erosion with masking image M respectively. The size of the circular structuring element is determined by its perimeter σ.

For $\sigma = 3$, circular objects of area $24.5\mu\text{m}^2$ or ellipsoidal objects with at least one axis smaller than $3.5\mu\text{m}$ are removed (Fig. 2, f). These values are well below the expected minimum area of totally damaged and rounded fibroblasts.

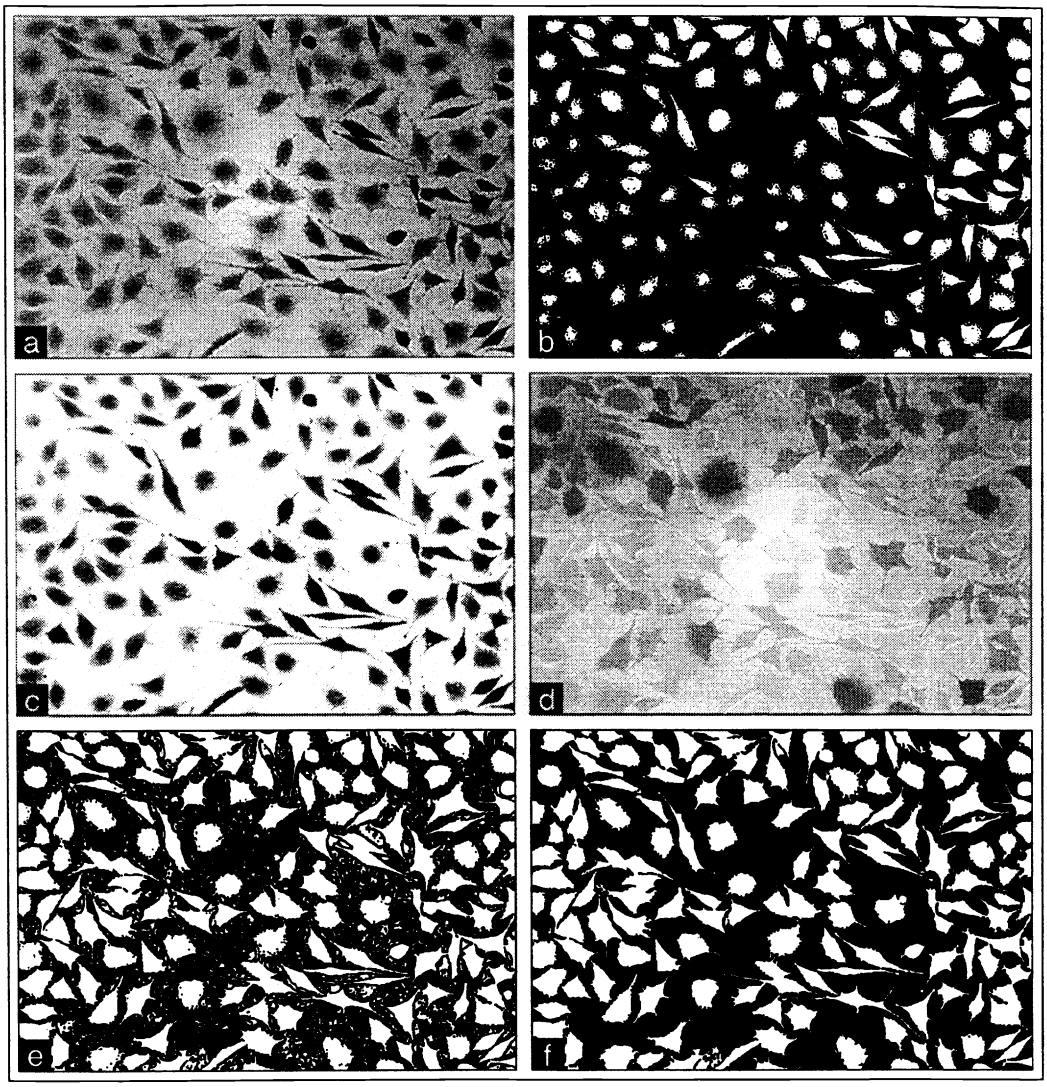

Figure 2. A micrograph $F(x,y)$ (a) is split into its object component $g - A(x,y)$ (c) and the illumination component $I(x,y)$ (c) by a log–tophat transform utilizing a closing–by–reconstruction. Compared to direct thresholding of $F(x,y)$(b), much better shapes are obtained by global thresholding of the absorption component $A(x,y)$ (e). Subsequent morphological noise removement perfectly yields cell shapes (f).

3.2. The multiscale segmentation algorithm

Progressive segmentation by reconstruction of object information from previously obtained markers is a common concept in mathematical morphology.[24] Since two cells touching each other can be separated best within their size–specific scale, a two–stage approach was developed. An image is initially decomposed into marker scales indicating the presence of particularly sized cells. After this *analysis stage* the original shapes are reconstructed, while the markers are prevented to merge again during the *synthesis stage* (Fig. 3).

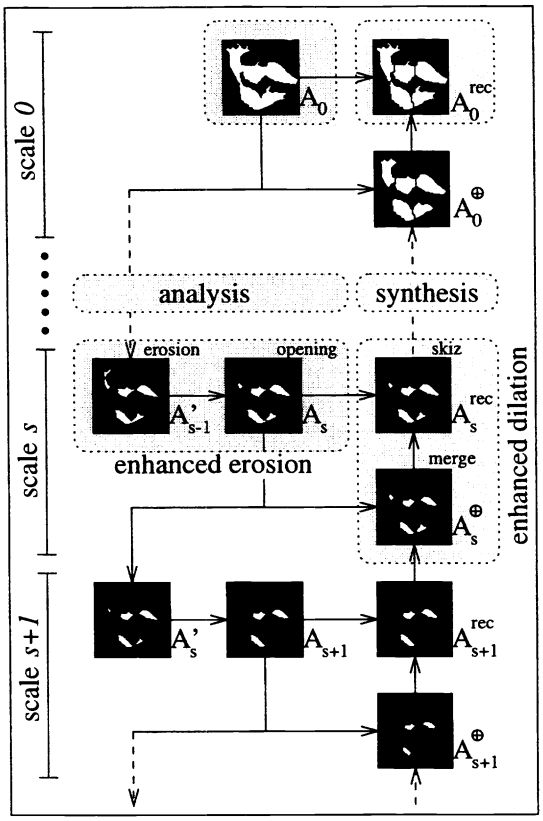

Figure 3. Scheme of the two–stage multiscale separation procedure. The analysis stage extracts separated markers for the cells by enhanced erosion. In the converse synthesis stage the enhanced dilation operator reconstructs original shapes of cells without merging separate markers.

Analysis by enhanced erosion. The binary image A_s represents the markers at scale $0 \leq s < s_{\max} \in \mathbb{N}$. The complete scale–space is generated by a cascade of $s_{\max} - 1$ successive enhanced erosions

$$A_{s+1} = \mathbf{D}_\sigma^m(\underbrace{\mathbf{E}_\sigma^n(A_s)}_{A_s''}, \underbrace{\mathbf{E}_\sigma^1(A_s)}_{M=A_s'}). \tag{6}$$

At scale s, the n–fold eroded image A_s $(= A'')$ is m–fold dilated and masked by the 1–fold eroded A_s $(= A')$, resulting in the next scale image A_{s+1} (Fig. 4). Each of these scale images introduces separations of those cells belonging to one specific scale.

The parameters n and m are derived from the estimation of cell size (Sec. 3.1). Likewise n–double reconstruction, the n–fold erosion filters false markers, and hence $n = 3$ is appropriate for all scales. Eqn. 6 actually represents an opening, so $m \geq n$ is an initial constraint for the m–fold dilation. For $m = n$ too many false markers remain from the n–fold erosion. The $(m = n + 1)$–fold dilation turned out to be a reasonable compromise between generation of false markers and correct segmentation of cells. The total number of scales $s_{\max}$ is a rather uncritical parameter as long as it is above a certain threshold depending on the maximum size of cells. For fibroblasts at magnification $\times 100$, a scale–space of $s_{\max} = 12$ proved sufficient.

Synthesis by enhanced dilation. The synthesis of marker scales A_s reconstructs the original cell shapes of A_0. At each scale s a reconstructed image A_s^{rec} is calculated, which incorporates the marker information of all scales $t \geq s$ and hence preserves their segmentations. These markers are reconstructed to the object size of scale s by combining A_{s+1}^{rec} and A_s such that $A_s \supseteq A_{s+1}^{\text{rec}}$. Therefore, the combined image $A_s^{\oplus}$ consists of all markers of A_{s+1}^{rec} and those occurring in A_s but not in A_{s+1}^{rec}:

$$A_s^{\oplus} = A_{s+1}^{\text{rec}} \cup \left\{ A_s \backslash A_{s+1}^{\text{rec}} \right\}. \tag{7}$$

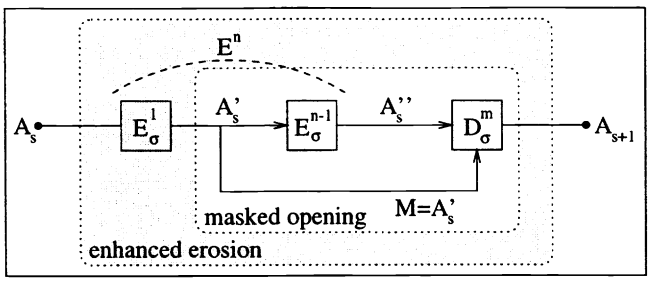

Figure 4. Enhanced erosion basically is an opening that consists of n–fold erosion and masked m–fold dilation. Since the constraint $m = n + 1$ proved useful, the operator is controlled by n, which exclusively depends on the minimum cell size.

This procedure ensures that no separation is lost during synthesis. The various inclusion relations between intermediate steps during segmentation are illustrated in Fig. 5. Finally, shapes of $A_s^{\oplus}$ are extended to those of A_s by a white skeleton–by–influence–zone[8] (skiz) yielding A_s^{rec}, i.e. the reconstructed markers of scale s:

$$A_s^{\text{rec}} = \mathbf{D}_\sigma^{\text{skiz}}(A_s^{\oplus}, A_s). \tag{8}$$

The white–skiz $\mathbf{D}_\sigma^{\text{skiz}}(A, M)$ differs from the reconstruction operator $\mathbf{D}_\sigma^{\infty}(A, M)$ by prohibiting separate objects to merge.[24] This results in a one–pixel gap between those objects in A covered by the same object in M, therefore the number of objects in $\mathbf{D}_\sigma^{\text{skiz}}(A, M)$ equals those in A. Basically, the white–skiz is the skeleton of the background and can be regarded as the binary analogon of the watershed transform for graylevel images.[25]

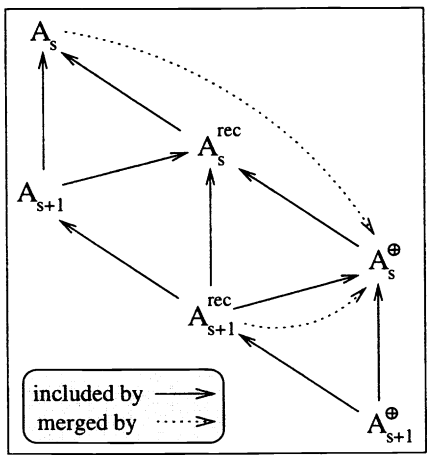

Figure 5. The inclusion relations of different intermediate marker images generated during multiscale segmentation are exemplified. From a set–theoretic point of view, the inclusion relation defines a partial ordering of the images.

Qualitative evaluation of the segmentation algorithm. Our algorithm was compared with other marker–based techniques for segmentation of connected binary objects (Fig. 6) by means of a synthetic image (a) and a part of a cytological microscopy (f). The corresponding distance transforms of the images are given in (b) and (g).

The segmentations shown in (c) and (h) were obtained from the ultimate eroded points of the binary sets. Additionally, the number of markers was reduced by opening to prevent extreme oversegmentation. Ideally, each cell is represented by one ultimate point indicating its center. The separation lines between the objects are determined to have maximum distance from all adjacent ultimate eroded points and are calculated by a white–skiz operation.[26] Two disadvantages of this approach can be noticed: (i) all objects have to be of similar size and (ii) all objects must exhibit regular shapes. Compact objects of different size are not segmented correctly because the marker generation is size– and scale–dependent (c). The number of markers, however, is correct in most cases. Objects with irregular shapes produce too many markers because the geometric interpretation is drawn from one scale only. This results in oversegmented images (h).

The second approach considers the (reduced) local maxima of the distance transform as initial markers.[27] The reconstruction of the actual shapes is done according to the descending values of the distance image by successive extension of the markers preventing merging. Although the distance transform is able to handle differently sized objects, irregular cells shapes still cause oversegmentation (i).

The demonstrated drawbacks of common algorithms result from their single–scale nature and are avoided by our multiscale approach. Morphological decomposition and converse stepwise reconstruction of markers is independent of the object's sizes and hence leads to improved segmentations of cell populations (k).

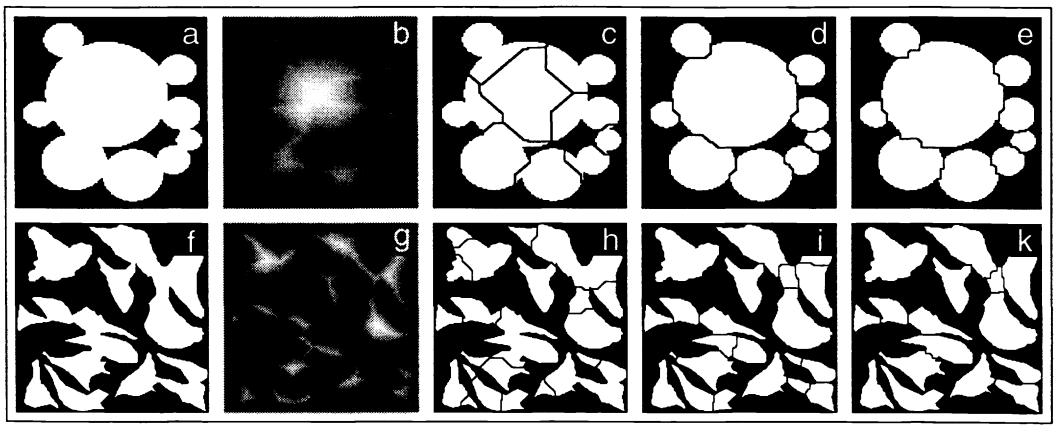

Figure 6. Synthetic image (a) and binarized micrograph (f) with their corresponding distance transforms (b, g). Reconstruction of filtered ultimate eroded points (c, h) yields rather poor results. By reconstruction of reduced local distance maxima (d, i) an acceptable result is achieved only for the synthetic image. The multiscale segmentation algorithm yields good results for the synthetic image (e) and improves results for the micrograph (k).

4. QUANTIFYING SHAPE DEFORMATION

Shape deformation, and hence, the toxicity of the substance under scrutiny is quantified by means of compactness distribution and pattern spectrum of the population. The measures were evaluated for different concentrations of two toxical reference substances.

4.1. Quantitative parameters

Compactness. Measurement of complex shape characteristics is done with respect to the application. Our goal is to quantify the extent, the presence of dendrides, and the degree of shape irregularity of fibroblast cells. A major requirement for a comprehensive shape parameter is rotation and translation invariance. Moreover, it is not sufficient to measure only the elongation of an object (as done by the aspect ratio). Because shape irregularities are most valuable characteristics to quantify cytotoxicity, a compactness value of binary objects measuring the cell's deviation from the ideal circle form, appears to be an appropriate parameter[20]:

$$C = \frac{4\pi \cdot \text{area}}{\text{perimeter}^2} \qquad \text{with} \qquad 0 \leq C \leq 1. \tag{9}$$

Pattern spectrum. Granulometric analysis of a binary pattern can be performed by means of its pattern spectrum. This morphological decomposition yields a distribution of increasing morphological primitives the given pattern consists of.[15] These pattern coefficients are obtained by successive opening with increasing convex structuring elements. This process can be regarded as sieving the pattern with different sieves resulting in a shape decomposition.[23] The size distribution

$$\Omega_A(i) := 1 - \frac{\#(\mathbf{O}_i(A))}{\#(\mathbf{O}_0(A))} \qquad i = 1, 2, 3, \cdots \tag{10}$$

yields the normalized number of pixels remaining in the image after an opening $\mathbf{O}_i$, with $\#(A)$ denoting the total number of object pixels in A. The discrete derivative of $\Omega(i)$ represents the pattern spectrum $d\Omega_A(i) = \Omega_A(i+1) - \Omega_A(i)$ of image A. Its coefficients represent weights of the morphological primitives the binary image A is composed of.

4.2. Cytotoxicity of SRMA and SRMB

The proposed method for micrograph segmentation and shape analysis was evaluated for fibroblast cells. The populations were treated with two toxical reference substances of different concentrations. All experiments were performed with $n = 3$, $m = 4$, and $s_{\max} = 12$.

SRMA and SRMB (standard reference materials) are toxic polymers with different toxicity. Both reference substances are made of polyurethane films containing various amounts of cytotoxic compounds.[28] All polymers, including the nontoxic control polymers (negative reference) were extracted under standard conditions (2cm^2 polymer/ml cell culture, time 72h, temperature 37°C). Extracts were then diluted to show dose dependent morphological changes to fibroblasts indicated by shrinking and rounding of cells. For both substances a negative reference population showing completely vital cells and a positive reference population showing completely damaged and deformed cells exemplify the cytotoxical range.

Since SRMA is more toxic than SRMB, the SRMA toxicity was tested for 10% and 20% concentration while SRMB was tested for concentrations of 50% and 100%. For both substances the compactness distributions were found to differ significantly by a Wilcoxon two–sample test. The four SRMA distributions "*negative*" ($\mu = 0.502$, $\sigma = 0.178$), 10% ($\mu = 0.632$, $\sigma = 0.161$), 20% ($\mu = 0.768$, $\sigma = 0.186$), and "*positive*" ($\mu = 0.824$, $\sigma = 0.152$) significantly differ ($p < 0.0001$). SRMB distributions "*negative*" ($\mu = 0.524$ $\sigma = 0.173$), 50% ($\mu = 0.619$, $\sigma = 0.159$), 100% ($\mu = 0.634$, $\sigma = 0.157$), and "*positive*" ($\mu = 0.799$, $\sigma = 0.143$) also differ significantly ($p < 0.0001$).

Compactness depends on area and perimeter of cells. For this, scatter plots also depict significant response to the different toxicity classes (Fig. 7). For visualization purpose 200 cells were arbitrarily chosen. Compactness, perimeter, and area behave monotonously for increasing toxicities, and hence correlate with the cytotoxicity of the used substance (Tab. 1). In addition, the *normalized compactness* states the relative compactness values in the range $[0; 1]$ between negative and positive control. By this, toxicity of different substances and results of different studies become comparable.

Because cytotoxical substances also influence sizes of vital fibroblasts, the pattern spectra of the various SRM populations were computed (Fig. 8). The results coincide with those of the compactness study (Tab. 1). As expected, the means of the pattern spectra (i.e. the dominating cell size) decrease for increasing toxicity. Furthermore, toxic populations become more homogeneous, which can be concluded from the monotonic decrease of standard deviation. These findings hold for both, SRMA and SRMB. Likewise normalized mean compactness, the normalized mean of pattern spectra yield figures enabling comparison of toxicity of different substances. For both normalized figures, SRMB toxicity is found to be much lower than SRMA toxicity, despite a concentration of five times compared to SRMA concentration.

	SRMA concentration				SRMB concentration			
	neg.	10%	20%	pos.	neg.	50%	100%	pos.
normalized mean compactness	0	0.404	0.826	1	0	0.345	0.400	1
compactness mean	0.502	0.632	0.768	0.824	0.524	0.619	0.634	0.799
perimeter mean	87.9	72.8	61.0	45.1	90.0	80.4	76.7	54.9
area mean	296.5	253.1	215.7	132.0	325.4	307.1	286.1	193.8
normalized mean pattern spectrum	0	0.495	0.708	1	0	0.044	0.293	1
pattern spectrum mean	8.65	7.21	6.59	5.74	8.01	7.93	7.47	6.17
pattern spectrum std. deviation	3.91	2.67	2.56	1.80	2.97	2.82	2.54	2.01

Table 1. Shape descriptors for SRMA and SRMB. Compactness distribution (*upper rows*) and pattern spectrum (*lower rows*) yield significant discrimination between toxicities. The normalized measures of both quantification methods indicate substantially higher toxicity for SRMA than for SRMB.

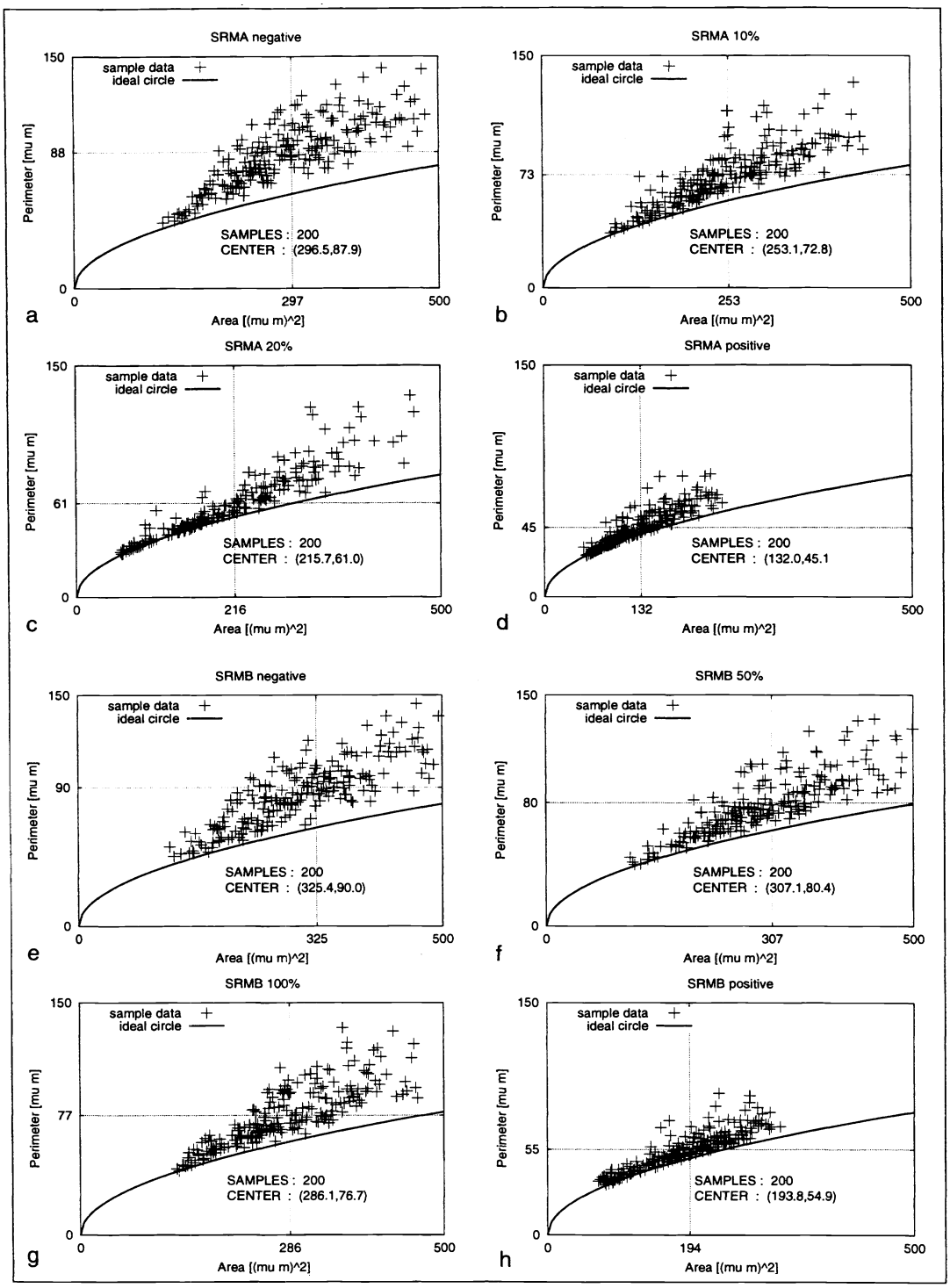

Figure 7. Cytotoxicity of SRMA and SRMB quantified by compactness distribution. The negative references (a and e) show vital cells, while the positive references (d and h) show totally damaged cells. SRMA concentrations 10% (b) and 20 % (c) lead to increasingly deformed cells. The toxic effects of the two SRMB concentrations 50% (f) and 100% (g) is also obvious from the diagrams.

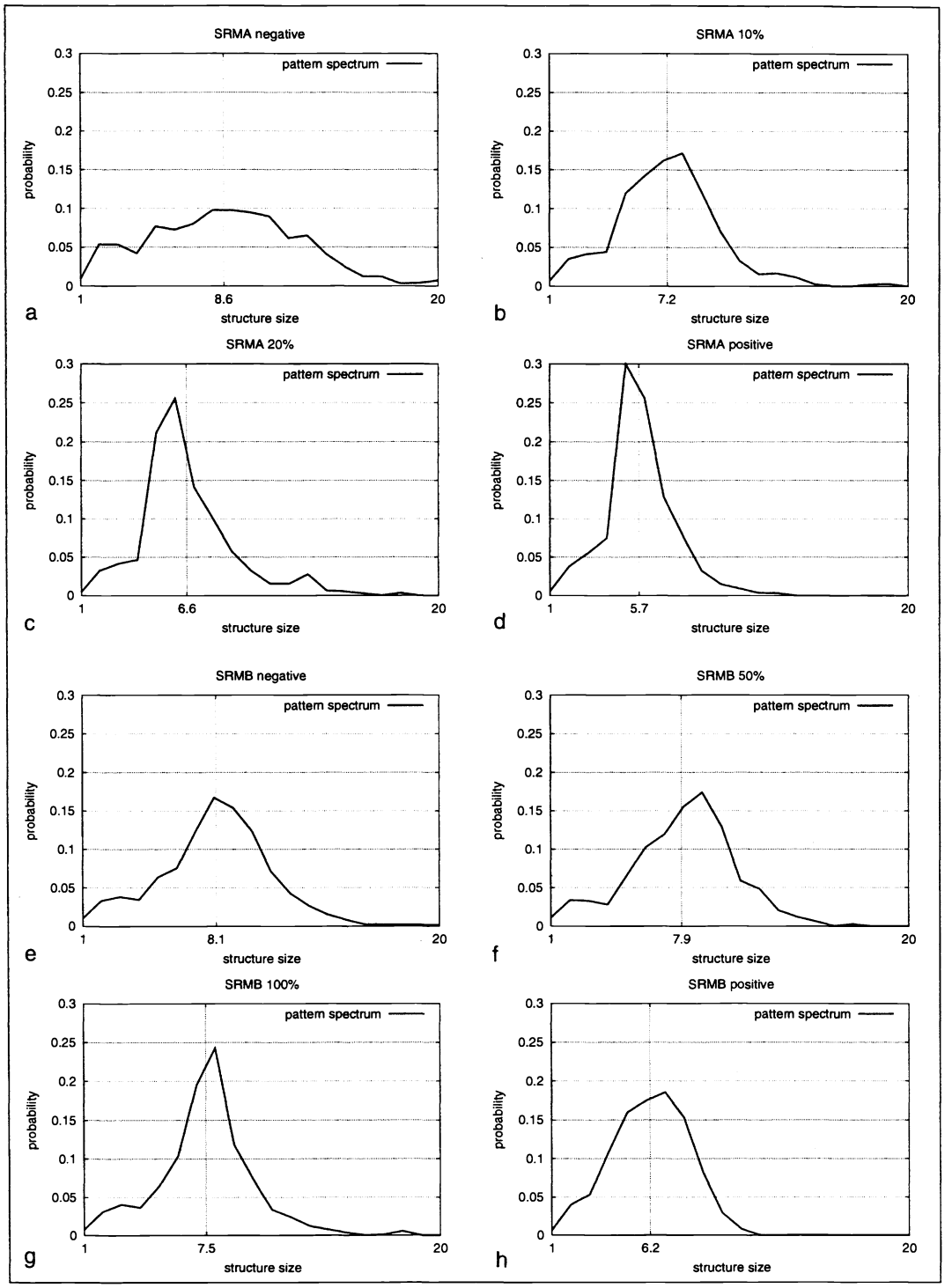

Figure 8. Cytotoxicity of SRMA and SRMB quantified by pattern spectra $\Omega_A(i)$ with $i = 1 \cdots 20$. Increasing cytotoxicity leads to decreasing mean and standard deviation of probability distributions for SRMA and SRMB. This corresponds to morphological changes of fibroblasts under toxic influence.

5. CONCLUSION

Discrimination between different phases of morphological change, and subsequent evaluation of toxicity of a biomaterial leads to a complex classification task. Since shape representation by only a few parameters is an enormous data compression, there exists no optimal single parameter carrying all aspects of shape.

For quantitative evaluation of biotoxicity we utilized a few characteristic shape descriptors yielding sufficient discrimination between basic phases of cytotoxicity. Our results allow for unique quantitative discrimination of cells under toxical influence. The experiments demonstrate the robustness of our method and statistical significance of the chosen parameters derived from compactness distribution and pattern spectrum of a population. Since our quantitative results correlate well with usual subjective visual inspection, we conclude that distributions of shape parameters acquired from automatically segmented micrographs are as robust and useful for biotoxicity assessment as are qualitative evaluations by experts. Hence, our method accounts for common verbal and qualitative descriptions of morphological cell changes.

Generally, the number of cells also indicates toxicity. However, due to adhesion effects cell concentrations usually vary heavily within the sample. This effect is even stronger for high toxicities. It therefore is an additional difficulty for expert segmentation to catch statistically meaningful groups of cells. This favors our computerized method, because all quantitative shape descriptors are independent of the number of cells. Furthermore, as demonstrated by reference results,[12] manually determined separations are also found automatically by our algorithm. Manually segmented cells generally are larger and have smoother appearance, but do not necessarily improve cell representation.

Commonly used separation algorithms require circular or similarly size objects, which are clearly inappropriate for analysis of cell populations. Our multiscale segmentation properly operates even for differently sized objects of very distinct shapes such as fibroblasts. Since all external control parameters can be estimated from cell sizes, the method may be adapted systematically to other monolayered cell populations. Our automatic method has several advantages over subjective examinations. E.g., quantitative cytotoxicity studies become comparable and laboratory staff is releaved from time consuming routine work. The obtained quantitative parameters were found to be statistically significant and are in excellent agreement with expert descriptions.[29] The method is currently in use for extensive clinical biotoxicity testing, in order to determine robust thresholds for toxicity of biomaterials.

ACKNOWLEDGMENTS

This work was partially supported by the German *Bundesministerium für Bildung und Forschung* (BMBF) under Grant No. 01ks9503/9. We thank Dr. Hans Bienert (BIOMAT, Aachen University of Technology, Germany) for providing the cytological samples.

REFERENCES

1. I. Young, "Quantitative microscopy," *IEEE Engineering in Medicine and Biology* **15**(1), pp. 59–66, 1996.
2. V. Metzler, J. Bredno, T. Lehmann, and K. Spitzer, "A deformable membrane for the segmentation of cytological samples," in *Medical Imaging*, vol. 3338 of *Procs. SPIE*, pp. 1246–1257, 1998.
3. G. Niederauer, T. Mac Gee, J. Keller, and R. Zaharias, "Attachment of epithelial cells and fibroblasts to ceramic materials," *Biomaterials* **15**(5), pp. 342–352, 1994.
4. M. Jourlin, "A model for logarithmic image processing," *Journal of Microscopy* **149**(1), pp. 21–35, 1988.
5. A. Oppenheim, R. Schaffer, and T. Stockham, "Nonlinear filtering of multiplied and convolved signals," *Proceedings of the IEEE* **56**(2), pp. 1264–1291, 1968.
6. D. Toth, T. Aach, and V. Metzler, "Illumination–invariant change detection," in *IEEE Southwest Symposium on Image Analysis and Interpretation*, (Austin, TX), April 2–4, 2000. In press.
7. V. Metzler, M. Puls, and T. Aach, "Restoration of ultrasound images by nonlinear scale–space filtering," in *Nonlinear Image Processing XI*, E. Dougherty and J. Astola, eds., vol. 3961 of *Procs. SPIE*, 2000. In the present volume.
8. P. Soille, *Morphological Image Analysis*, Springer–Verlag, Berlin, 1999.
9. Q. Wei, C. Reme, and P. Stucki, "Advanced image processing and modeling system for the analysis of cell micrographs in morphology," in *Biomedical Image Processing and Biomedical Visualization*, vol. 1905 of *Procs. SPIE*, pp. 175–185, 1993.

10. A. Elmoataz, S. Schupp, R. Clouard, P. Herlin, and D. Bloyet, "Using active contours and mathematical morphology tools for quantification of immunohistochemical images," *Signal Processing* **71**(2), pp. 215–226, 1998.
11. S. Portet, J. Vassy, M. Beil, G. Millot, A. Hebbache, J. Rigault, and D. Schoevaert, "Quantitative analysis of cytokeratin network topology in the MCF7 cell line," *Cytometry* **35**(3), pp. 203–213, 1999.
12. V. Metzler, T. Lehmann, H. Bienert, K. Mottaghy, and K. Spitzer, "Scale–independent shape analysis for quantitative cytology using mathematical morphology," *Computers in Biology and Medicine* , 2000. In press.
13. P. Maragos and R. Schaffer, "Morphological filters – part II: Their relation to median, order–statistic, and stack filters," *IEEE Transactions on Acoustics, Speech, and Signal Processing* **35**(8), pp. 1170–1184, 1987.
14. H. Heijmans, "Mathematical morphology as a tool for shape description," in *Shape in Picture: Mathematical Description of Shape in Grey-level Images*, Y.-L. O, A. Toet, D. Foster, H. Heijmans, and P. Meer, eds., pp. 147–176, Springer–Verlag, Berlin, 1994.
15. P. Maragos, "Pattern spectrum and multiscale shape representation," *IEEE Transaction on Pattern Analysis and Machine Intelligence* **11**(7), pp. 701–716, 1989.
16. J. Reinhardt and W. Higgins, "Comparison between the morphological skeleton and morphological shape decomposition," *IEEE Transactions on Pattern Analysis and Machine Intelligence* **18**(9), 1996.
17. P. Salembier and M. Kunt, "Size–sensitive multiresolution decomposition of images with rank–order based filters," *Signal Processing* **27**, pp. 205–241, 1992.
18. J. Goutsias and H. Heijmans, "Multiresolution signal composition schemes. Part 1: Linear and morphological pyramids," Tech. Rep. CWI PNA–R9810, National Research Institute for Mathematics and Computer Science, Amsterdam, 1999.
19. T. Lehmann, A. Sovakar, W. Schmitt, and R. Repges, "A comparison of similarity measures for digital subtraction radiography," *Computers in Biology and Medicine* **27**(2), pp. 151–167, 1997.
20. J. Russ, *Computer–Assisted Microscopy*, Plenum Press, New York, 1990.
21. K. Skifstad and R. Jain, "Illumination independent change detection for real world image sequences," *Computer Vision, Graphics, and Image Processing* **46**, pp. 387–399, 1989.
22. C. Moloney, "Methods for illumination–independent processing of digital images," in *IEEE Pacific Rim Conference on Communications, Computers, and Signal Processing*, pp. 811–814, 1991.
23. E. Dougherty, *An introduction to morphological image processing*, SPIE Press, Bellingham, WA, 1992.
24. F. Meyer and S. Beucher, "Morphological segmentation," *Journal of Visual Communication and Image Representation* **1**(1), pp. 21–46, 1990.
25. C. Orbert, E. Bengtsson, and B. Nordin, "Watershed segmentation of binary images using distance transformations," in *Nonlinear Image Processing IV*, vol. 1902 of *Procs. SPIE*, pp. 159–170, 1992.
26. J. Serra, *Image Analysis and Mathematical Morphology*, Academic Press, London, 1982.
27. G. Borgefors, "Distance transforms in digital images," *Computer Vision, Graphics and Image Processing* **34**, pp. 679–698, 1986.
28. T. Tsuchiya, "Studies on the standardization of cytotoxicity tests and new standard reference materials useful for evaluating the safety of biomaterials," *Journal of Biomaterial Application* **9**(2), pp. 138–157, 1994.
29. V. Metzler, H. Bienert, T. Lehmann, K. Mottaghy, and K. Spitzer, "A novel method for quantifying shape deformation applied to biocompatibility testing," *ASAIO Journal* **45**(4), pp. 264–271, 1999.